



Cite this: *Chem. Soc. Rev.*, 2015, 44, 1791

Recent advances in Gd-chelate based bimodal optical/MRI contrast agents†

Peter Verwilst, Soyeon Park, Byungkwon Yoon and Jong Seung Kim*

Research on bimodal contrast agents in general and optical/MRI contrast agents in particular has attracted increased attention from the scientific community in recent years. Whereas optical contrast agents reveal pathologies at the cellular or sub-cellular level, MRI contrast agents generally report physiological differences at the level of tissues and organs. The complementary information obtained from these two techniques allows for a more precise diagnosis. Furthermore the emergence of near-infrared luminophores accommodates the simultaneous detection of optical and MRI signals. The current multitude and diversity in molecular architectures mirrors the ever increasing interest in the field. In this review the developments between 2010 and mid-2014 are highlighted.

Received 9th October 2014

DOI: 10.1039/c4cs00336e

www.rsc.org/csr

Key learning points

- 1 Which parameters govern Gd³⁺-chelate based MRI contrast agents?
- 2 What are the currently researched molecular architectures of bimodal optical/MRI contrast agents?
- 3 How does the chosen architecture influence the MRI properties?

1. Introduction

1.1. MRI, relaxivity and T₁ contrast agents

Magnetic resonance imaging (MRI) has become a routinely used diagnostic tool in hospitals worldwide, owing to the deep tissue penetration of this imaging technique. Whereas the image resolution of MRI is superior to other tissue penetrating imaging techniques such as positron emission tomography (PET) or single-photon emission computed tomography (SPECT), it is still limited to detecting disparities in magnetic properties of tissues and organs in the clinical practice. The resolution of MRI images is related to the magnetic field strength of the MRI magnet, and as high field MRI detectors are currently being developed, the resolution of MRI images is continuously improving. The contrast induced by gadolinium based contrast agents is also field dependent (see later), and their efficiency is greatly reduced at very high field strengths. In this regard, if the use of external inducers of MRI contrast is needed, the lack of sensitivity of the contrast agent in high field MRI machines may outweigh the advantages of a higher resolution image.

Optical techniques on the other hand allow for the detection of variations in luminescence emission intensities at cellular or sub-cellular levels. Living tissues are not very transparent to light of wavelengths shorter than ± 650 nm, due to the light absorbing properties of life-associated chromophores such as haemoglobin and melanin. Light of shorter wavelengths can be very useful in detecting pathologies in *ex vivo* tissue slices, yet luminophores emitting light with wavelengths in the red and near infrared (NIR) regions of the electromagnetic spectrum can be used to detect light *in vivo*, and are more and more becoming the subject of intensive investigations. Despite the higher transparency of tissues to light with wavelengths longer than 650 nm, for light to travel into tissues, be absorbed and then light of a longer wavelength to be emitted and detected, a penetration level of only a few cm can be attained. Whole body imaging therefore is mainly limited to small rodents, even though human whole body imaging can in some cases be realised. This limitation however does not necessarily preclude optical imaging to be applicable to humans, as many vital organs can readily be reached using fiberoptics.

Due to the physical limitations associated with every individual imaging technique, it is unlikely that a single technique will be suitable for all purposes. Rather, the combination of two or more complementary techniques should lead to broad applicability. The combination of MRI and optical methods,

Department of Chemistry, Korea University, Seoul 136-701, Korea.

E-mail: jongskim@korea.ac.kr; Fax: +82-2-3290-3121

† Electronic supplementary information (ESI) available. See DOI: 10.1039/c4cs00336e

for the reasons described above, is one of those complementary techniques under current investigation, and could soon become a routinely used research tool itself, as commercial detectors allowing the simultaneous detection of MRI and optical signals (for small animals) are being realised.

Here, we will discuss the current major developments in the field of bimodal MRI/optical contrast agents in the 2010 to mid-2014 time period, grouped by the morphology and light emitting source, prior developments have been reviewed elsewhere.¹

In the following section, the technique of magnetic resonance imaging and the use of MRI contrast agents will briefly be described. Currently many different types of contrast inducing species have been investigated, ranging from paramagnetic nanoparticles over metal complexes of Mn^{2+} , Eu^{2+} and Gd^{3+} ; as well as other lanthanides in the case of saturation transfer contrast agents. Here, we will limit the discussion to gadolinium chelate based MRI contrast agents. As these gadolinium based contrast agents have been found to be most useful as longitudinal relaxation (T_1) contrast agents, we will limit the following discussion to T_1 contrast enhancement. We direct the reader to a number of excellent source materials for further reading.²

A T_1 -weighted MRI image is a three-dimensional representation of the longitudinal relaxation time of protons (of mainly

water molecules) contained in tissues. In the image, short relaxation times appear bright and longer relaxation times appear dark. In some cases this natural contrast is adequate for diagnostic purposes, however, frequently magnetically identical sections of an MRI image might be histologically distinct. In those cases, the addition of a contrast agent induces an expedited T_1 relaxation and thus a brighter image.

It was observed that the addition of a paramagnetic agent increases the proton T_1 relaxation rate of the solution it is added to. Owing to its seven unpaired electrons, the largest number of all the elements in the periodic table, combined with a long electronic relaxation time, Gd^{3+} ions induce the largest effect compared to other paramagnetic ions.

Despite this advantageous property, gadolinium ions cannot be used as free ions, due to their elevated toxicity. In order to overcome this hurdle, organic ligands, tightly binding a single gadolinium ion, have been developed. Most contrast agents, in particular those based on the cyclic DOTA ligand, and DTPA, its acyclic analogue (Fig. 1), consist of 8 donor atoms, allowing one water molecule to directly interact with the 9-coordinate gadolinium ion. Those water molecules are known as the inner sphere water molecules (Fig. 2). The water molecules not directly bound to the gadolinium ion, but rather being hydrogen bonded to the ligand,



Peter Verwilt

Peter Verwilt was born in Leuven, Belgium, in 1985. He received his PhD from the University of Leuven, Belgium, under the supervision of Prof. W. Dehaen and Prof. W. De Borggraeve in 2011. He subsequently joined the research group of Dr N. McClenaghan at the Univeristé Bordeaux 1/CNRS, France, and in 2013 he joined the group of Prof. J. S. Kim as a research professor. His research interests include theranostic targeted drug delivery and bio-(in)organic sensors.



Soyeon Park

Soyeon Park was born in Jeonju, Korea, in 1989. She received her Bachelor degree from the Department of Chemistry at Korea University in 2013. She obtained a Master degree under the guidance of Prof. J. S. Kim. Her research focuses on small pH-activatable probes for drug delivery and imaging.



Byungkwon Yoon

Byungkwon Yoon was born in Seoul, Korea, in 1987. He received his Bachelor degree from the Department of Chemistry at Korea University 2013. He has been awarded his Master degree under the guidance of Prof. J. S. Kim. His main research theme is the design and synthesis of fluorogenic chemosensors.



Jong Seung Kim

Jong Seung Kim was born in Daejeon, Korea in 1963. He received a PhD from the Department of Chemistry and Biochemistry at Texas Tech University. After a one-year post-doctoral fellowship at the University of Houston, he joined the faculty at Konyang University in 1994 and transferred to Dankook University in 2003. He moved to Korea University in 2007. To date, his research records 336 scientific publications and 50 domestic and international patents.

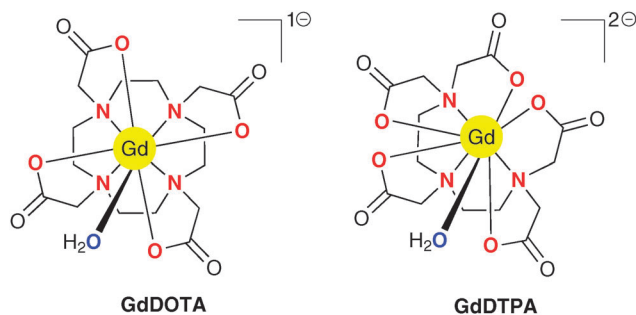


Fig. 1 Chemical structures of GdDOTA and GdDTPA, donor atoms are depicted in red, the coordinated water in blue.

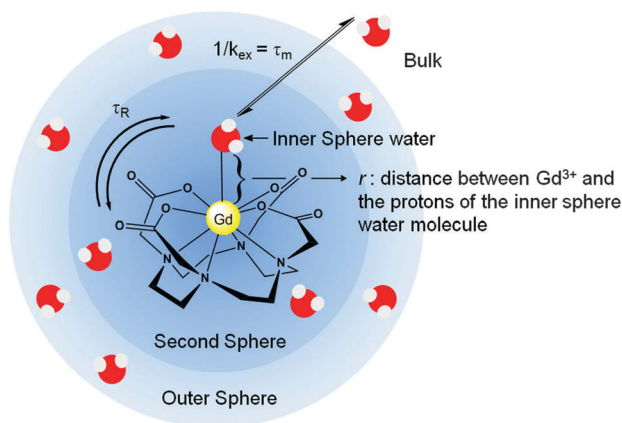


Fig. 2 A graphical representation of the factors influencing a contrast agent's relaxivity. (Abbreviations: see main text.)

comprise the second sphere, and all other water molecules, not part of the first and second coordination sphere, but still exerting an effect on the relaxation rate are the outer sphere water molecules (Fig. 2).

The shortened observed relaxation rate ($1/T_{1,obs}$) upon the addition of a paramagnetic species can be described as the sum of the relaxation rate in the absence of the paramagnetic ion ($1/T_{1,d}$) and the influence of the said paramagnetic ion ($1/T_{1,p}$). The latter one was observed to be linearly dependent on the concentration of the paramagnetic contrast agent (CA); the specific concentration independent factor characterising this paramagnetic agent is known as the relaxivity (r_1), as described in eqn (1). The paramagnetic contribution to the relaxation rate ($1/T_{1,p}$) is the sum of contributions from the inner-sphere water molecules, in immediate contact with the paramagnetic agent, and the contributions from the second sphere and outer sphere water molecules (denoted by the superscripts IS, SS and OS respectively; eqn (2)). Even though the second and outer sphere water molecules are not directly bound, they do represent a significant contribution to the relaxivity, especially so in small contrast agents with low hydration numbers (q , the number of inner-sphere water molecules) For example, in GdDOTA and GdDTPA, the second and outer sphere terms contribute to roughly half of the observed relaxivity.

The inner-sphere contribution can be described by the Solomon–Bloembergen–Morgan equations, a simplified form

of which can be seen in eqn (3) and (4). T_{1M} is the longitudinal relaxation correlation time of the bound water molecule and τ_m is the reciprocal of the water exchange rate (k_{ex}) of the bound water molecule with the bulk water (Fig. 2). T_{1M} can be further divided into a scalar (SC) and a dipole-dipole (DD) contribution, arising from electronic interactions and nuclear interactions respectively.

$$\frac{1}{T_{1,obs}} = \frac{1}{T_{1,d}} + \frac{1}{T_{1,p}} = \frac{1}{T_{1,d}} + r_1[CA] \quad (1)$$

$$\frac{1}{T_{1,p}} = \frac{1}{T_{1,p}^{IS}} + \frac{1}{T_{1,p}^{SS}} + \frac{1}{T_{1,p}^{OS}} \quad (2)$$

$$\frac{1}{T_{1,p}^{IS}} = \frac{[CA]}{55.56} \frac{q}{(T_{1M} + \tau_m)} \quad (3)$$

$$\frac{1}{T_{1M}} = \frac{1}{T_{1M}^{SC}} + \frac{1}{T_{1M}^{DD}} \quad (4)$$

In the case of the most contrast agents of practical use, $\tau_m \ll T_{1M}$, thus simplifying eqn (3) to eqn (5). At higher field strengths ≥ 0.25 T (≥ 10 MHz), the scalar interactions become very small and eqn (4) can be simplified to eqn (6). The contribution of the dipole-dipole interactions to the relaxation rate is also field-dependent as expressed in eqn (6) where ω_L is the proton Larmor frequency (42.58 MHz T^{-1}). The sum of the water exchange rates ($k_{ex} = 1/\tau_m$) and the tumbling rate ($1/\tau_R$) in eqn (7) is dominated by the tumbling rate in most small contrast agents. For example DOTA exhibits a τ_m of 243 ns and a τ_R of 53 ps. Combining eqn (5)–(7), for a rapidly tumbling contrast agent, it can be seen that the inner sphere contributions to the relaxivity can be dramatically increased simply by prolonging τ_R (slower rotation). At slower rotation rates, the water exchange rate becomes a limiting factor as well. As the $\omega_L^2 \tau_{cl}^2$ term from eqn (6) becomes much more significant at field strengths over ≥ 0.25 T, the influence of a slower tumbling rate becomes much more pronounced in this region, as can be seen from Fig. 3.

$$\frac{1}{T_{1,p}^{IS}} = \frac{[CA]q}{55.56 T_{1M}} \quad (5)$$

$$\frac{1}{T_{1M}} = \frac{1}{T_{1M}^{DD}} \propto \frac{3\tau_{cl}}{(1 + \omega_L^2 \tau_{cl}^2)} \quad (6)$$

$$\frac{1}{\tau_{cl}} = \frac{1}{\tau_m} + \frac{1}{\tau_R} \quad (7)$$

The relaxivity of MRI contrast agents can be modulated upon the encounter of an external stimulus,³ as will be shown below using literature examples. The most frequently used strategies are the (non)-covalent interaction of a small MRI contrast with a large molecule resulting in a slower tumbling rate of the conjugate and thus an increased relaxivity, especially so at field strengths corresponding to the 10–500 MHz range, according to eqn (5)–(7) and Fig. 3. Or by changing the number

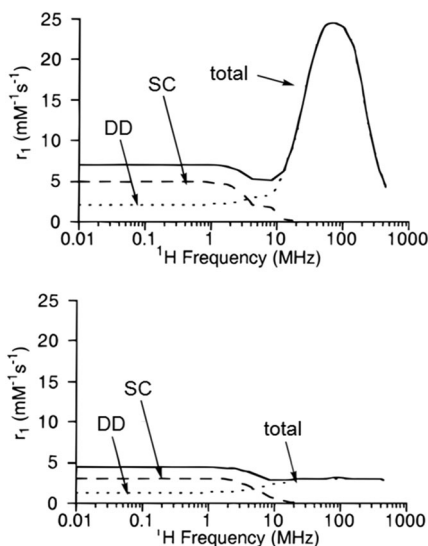


Fig. 3 The influence of the scalar (SC) and dipole–dipole (DD) interactions on the calculated inner sphere relaxivities top: $\tau_R = 1$ ns, bottom: $\tau_R = 0.1$ ns. Adapted with permission from ref. 2a. Copyright 1999 American Chemical Society.

of inner-sphere water molecules (q), which results in a linear increase in relaxivity, independent of field-strength as described in eqn (3), in a process known as q -modulation.

1.2. Biological considerations

As mentioned before, free gadolinium ions are highly toxic, the toxicity arises from the gadolinium ion's ability to displace calcium ions in many biologically important peptides and enzymes, resulting in the inhibition of their function. For this reason, for a contrast agent to be clinically approved, the contrast agent not only has to exhibit a high thermodynamic equilibrium constant but also has to show kinetic inertness. Upon the injection of a contrast agent in the blood stream, metal ions, in particular zinc ions, will compete with gadolinium and this results in the release of small doses of free gadolinium ions.⁴

Even clinically approved contrast agents have in recent years been demonstrated to carry an increased risk for the development of nephrogenic systemic fibrosis (NSF), a potentially lethal disease characterised by the thickening of skin and scar tissue formation in vital organs such as heart, lungs, liver and kidneys. Most small molecule contrast agents are excreted from the body *via* renal clearance, therefore patients with renal diseases, exhibiting lower clearance rates, are particularly at risk of developing NSF, as more gadolinium ions will be displaced from their chelates due to an increased circulation time.⁴

In view of these facts, the toxicity of contrast agents must always be taken into consideration when developing new contrast agents. Rapid renal clearance of contrast agents from the blood is not always possible, for example in the case of blood pool MRI contrast agents (MRI contrast agents non-covalently attached to a blood protein, in order to ensure an intravascular bio-distribution) significantly longer blood circulation times

have been recorded.⁴ Therefore these contrast agents are generally administered in lower doses. Alternatively contrast agents may be substituted with functional groups increasing hepatobiliary excretion rates, thus circumventing the renal pathway.

Whereas MRI contrast agents can in theory be used to detect any kind of target, granted that the appropriate ligand has been attached, the biological confinement of the target needs to be considered as well. As contrast agents are usually injected in the blood stream, biological barriers need to be conquered in order for the contrast agent to reach its goal. This is certainly so if the contrast agent's target is located intracellularly. Whereas some of these intracellular contrast agents show quite promising and remarkable results (see later), the presumed severe toxicity arising with the associated increased circulation times, as well as the decreased stability of MRI contrast agents in acid media, such as can be found in lysosomes, may ultimately limit their applicability. Future endeavours in designing contrast agents directed to confined biological spaces (*e.g.* intracellular, intracranial, *etc.*) must therefore include efficient clearance modalities for clinical applications to be viable.

Not only the MRI contrast agent but also the luminophore may present unique challenges as far as biological compatibility is concerned. For example, to the best of our knowledge, only 2 organic fluorophores exhibiting emission at wavelengths above 650 nm have yet been FDA (U.S. Food and Drug Administration) approved, namely methylene blue and indocyanine green. The inorganic fluorophores can exhibit additional toxicity associated with heavy metal cations.

2. Discrete molecules

2.1. Organic fluorophores

The most straightforward way to achieve the synthesis of a bimodal contrast agent is by attaching a small organic fluorophore to one of the pendant arms of a MRI contrast agent. Many such contrast agents have been described in the past and we direct the reader to prior reviews summarising the achievements described before 2010.¹

Two recent examples expanding on this strategy consist of a DOTA based contrast agent bearing a ligand for a cell surface receptor on one of the complex's arms and biotin on the opposing arm.⁵ The biotin appended contrast agent **1** was proven to be an excellent bimodal contrast agent for these surface receptors upon the addition of a commercially available avidin–dye conjugate (Fig. 4). Here the well-known specificity and high affinity of the avidin–biotin couple was used to introduce a fluorescent moiety. Contrast agent **1b** (Fig. 5) shows an increase in the cellular relaxation rates ($R_{1,\text{cell}} = 1/T_{1,\text{cell}}$) of 36% upon binding to its target receptor.^{5b} Despite these impressive results it should also be noted that biotin can increase cellular uptake *via* receptor mediated endocytosis, and further long term toxicological studies would be necessary to determine the applicability of this novel way to achieve bimodal imaging.

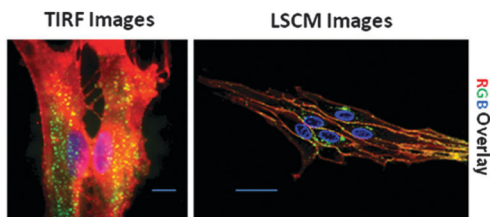


Fig. 4 Overlay of images of live mGluR5 expressing secondary astrocytes after labeling with **1b** (10 μM for 10 min) and Avidin Alexa-Fluor488 (green). Cell membranes were stained with CellMask Orange (red) and nuclei with Hoechst 33342 (blue). Bar size is 11 μm in the TIRF images, and 30 μm in the LSCM images. Reprinted with permission from ref. 5b. Copyright 2014 American Chemical Society.

Another example consists of a peptidic ligand for a particular blood-borne protein, *in casu* fibrin, decorated with a DO3A mono amide based MRI contrast agent and fluorescein at opposing ends of the peptide. Owing to the slower rotation upon binding fibrin, contrast agents **2a** and **2b** showed an increase in their r_1 values (1.4 T, 37 $^\circ\text{C}$) by 30% and 50% respectively.⁶

Furthermore, fluorophores can double as ligands targeting specific biological interactions themselves, thus eliminating the need for double substitution of MRI contrast agents.

Examples include the use of 3-(*p*-dimethylaminophenyl)-coumarin for the detection of myelination (**3**),⁷ curcumin (**4**)⁸ and 4-(6-methoxy-1,3-benzothiazol-2-yl)aniline (**5**)⁹ for the early detection of Alzheimer's disease and 1,4- and 1,5-disubstituted anthraquinones targeting calf thymus DNA (**6**).¹⁰ In addition to being target selective fluorescent ligands, many of these fluorophores exhibit a turn-ON fluorescent behaviour upon binding their respective receptors.

Bound to their receptors, the intramolecular rotational freedom of the fluorophores is restricted, leading to smaller percentages of non-radiative decay and thus an increase in the fluorescence quantum yield. This dual modulation of signal intensities (increase in relaxation rate as well as fluorescence enhancement) upon binding a target, is highly desirable for a contrast agent in order to maximise its potential as a bimodal contrast agent.

In the case of the myelin specific contrast agent **3**, the r_1 value of 5.8 $\text{mM}^{-1} \text{s}^{-1}$ at 0.47 T and 40 $^\circ\text{C}$ corresponds well with the size of the molecule.^{7b} The fluorescence of brain slices treated with complex **3** showed a good overlap with known myelin staining agents, proving the specificity of the contrast agent. Upon intraventricular injection, the contrast agent was able to bind myelinated fibers *in vivo*, allowing the detection of demyelinated lesions by T_1 mapping (Fig. 6).⁷ These data

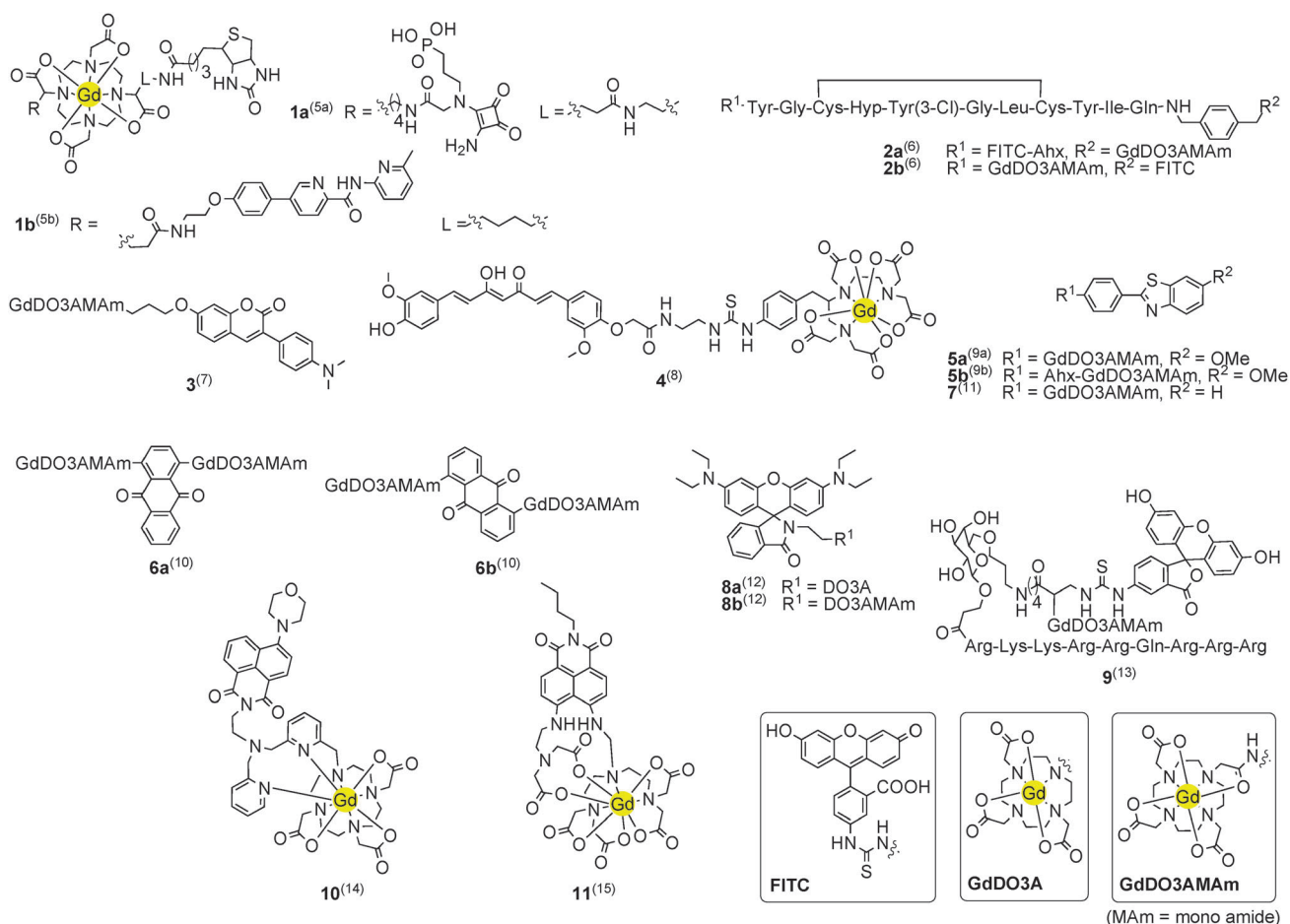


Fig. 5 Structures of the organic fluorophore appended MRI contrast agents **1–11**.^{5–15} (References between brackets.)

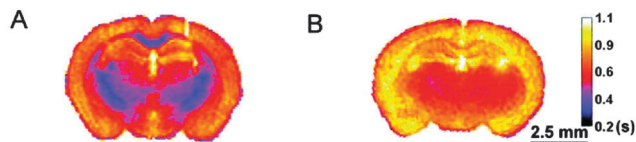


Fig. 6 Representative MR T_1 maps of wild-type (A) and shiverer (B) mouse brain tissues treated with **3**. Reprinted with permission from ref. 7b. Copyright 2011 American Chemical Society.

represent a major advancement in the detection of demyelinating diseases, however as this contrast agent has to be injected intracranially, retention of the contrast agent, and toxicity associated therewith, could be anticipated.

The curcumin conjugated DTPA complex **4** (ref. 8) and a series of 4-(6-methoxy-1,3-benzothiazol-2-yl)aniline conjugated DO3A mono amide complexes (**5**)⁹ showed selective labelling of β -amyloid plaques, one of the hallmarks of Alzheimer's disease, by monitoring the fluorescence (increase). As the recognition of the β -amyloid plaques requires a large hydrophobic molecule, the contrast agents tend to self-aggregate above the critical micellar concentration (cmc). Whereas cmc values in the range of 1–2 mM were reported for **5a** and **5b**, **4** presumably underwent self-assembly as well, as can be judged from the r_1 values of $13.63 \text{ mM}^{-1} \text{ s}^{-1}$ of a pH 7.4 buffered solution at 1.4 T and 37°C , which is higher than the r_1 value that would be expected of a contrast agent with a molecular weight of a single molecule of **4**. The r_1 value of **4** also corresponds well with the reported r_1 above the cmc of complexes **5a** and **5b**, around $13 \text{ mM}^{-1} \text{ s}^{-1}$ and $11 \text{ mM}^{-1} \text{ s}^{-1}$ under similar conditions.^{8,9} Whereas complexes **4** and **5** represent an important advancement in the development of contrast agents targeting neurological diseases, the inability to cross the blood–brain barrier, a tightly regulated boundary between the brain and circulating blood, in sufficient concentrations, limits the clinical application of these contrast agents and represents a hurdle that yet needs to be surmounted.

The anthraquinone based contrast agents **6a** and **6b** were designed to study the interaction with DNA. Contrary to other 1,4- and 1,5-disubstituted anthraquinones, the affinity for duplex DNA was higher for the 1,4-disubstituted contrast agent (**6a**). A likely explanation for this behaviour is that the 1,5-disubstituted anthraquinone's bulkiness causes the intercalation in the sparring binding mode to be kinetically inaccessible. As a consequence the 1,4-disubstituted isomer experiences the strongest binding. Upon binding DNA, the observed molecular r_1 increased by 116% from $5.4 \text{ mM}^{-1} \text{ s}^{-1}$ to $11.7 \text{ mM}^{-1} \text{ s}^{-1}$ for **6a** and by 79% from $7.2 \text{ mM}^{-1} \text{ s}^{-1}$ to $12.9 \text{ mM}^{-1} \text{ s}^{-1}$ for **6b**.¹⁰

By using benzothiazole aniline for tumour targeting (**7**),¹¹ Kim *et al.* advanced beyond using a fluorescent ligand for targeting purposes, as the fluorescent molecule itself also serves as an anticancer drug. The r_1 value of $3.84 \text{ mM}^{-1} \text{ s}^{-1}$ corresponds well to the molecule's size. Upon active uptake into several cancer cell lines, the complex was clearly present in both the cytosol and the nuclei of these cells as can be seen from the T_1 weighted MR images (Fig. 7). The parent benzothiazole aniline is known to be a potent anticancer drug, its biological action arising from the formation of covalent DNA

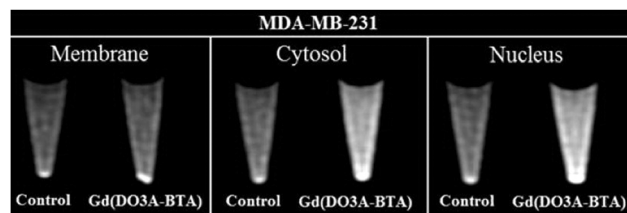


Fig. 7 T_1 -weighted MR images of MDA-MB-231 cell fractions incubated with **7** vs. untreated cells. Reprinted with permission from ref. 11. Copyright 2013 American Chemical Society.

adducts. When conjugated to a Gd–DO3A mono amide core, the biological action of the benzothiazole aniline remains preserved. When mice, xenografted with MDA-MB-231 tumours, were treated with the contrast agent, a significant growth inhibition was observed in the tumour growth curves. The contrast agent seems to be well tolerated up to 21 days of daily injections of a 1 mmol kg^{-1} dose. Long term toxicity studies will however be necessary to assess the safety of the theranostic drug.

Rhodamine B conjugates with DO3A (a DOTA-type ligand in which one coordinating carboxylate is substituted by a non-coordinating group) (**8a**) or DO3A mono amide (**8b**) exhibit pH-modulated fluorescence.¹² Under acidic conditions the spirolactam is opened resulting in an increased fluorescence. Whereas the bis-hydrated DO3A conjugate showed a r_1 of $8.5 \text{ mM}^{-1} \text{ s}^{-1}$ at 9.4 T and 25°C , the monohydrated DO3A mono amide conjugate displayed a r_1 of only $3.8 \text{ mM}^{-1} \text{ s}^{-1}$ under identical conditions. Despite the elevated relaxivity of **8a**, the low water-solubility prevented its further applications. DO3A mono amide conjugate **8b** was able to undergo cellular uptake in cultured cells and is presumed to exhibit mitochondrial localisation, similar to the parent compound, rhodamine B. *In vivo* studies revealed the selective tumour uptake in xenografted nude mice due to the more acidic extra- and intracellular pH associated with the increased metabolism of tumours. Furthermore the fluorescence of **8b** was switched on in the acidic tumour cells, but not in healthy cells, allowing for the discrimination between cancerous and normal cells.

Cellular uptake and retention can be used as a method for contrast enhancement as well. Conjugate **9** consists of a Gd–DO3A mono amide complex in which one of the acetate groups was reacted with a lysine chain, thus paving the way for a dual substitution with a fluorescein molecule as well as a gallactose unit.¹³ The gallactose unit was further derivatised with a cell penetration peptide (CPP), facilitating cellular uptake. The conjugate was designed so that the CPP would be cleaved off by β -galactosidase (β -gal), resulting in cellular retention in β -gal expressing cells. The conjugate was shown to have a r_1 of $16.8 \pm 0.6 \text{ mM}^{-1} \text{ s}^{-1}$ at 2.9 T and 21°C , which was attributed to the slower tumbling rate of this bulky molecule. An increased cellular retention was shown both by more intense fluorescence as well as an elevated $R_{1,\text{cell}}$, despite the fact that the cleavage of the CPP results in a smaller molecule and accordingly should thus also exhibit a smaller r_1 vs. the uncleaved conjugate. This observation demonstrates that, in order to achieve increased $R_{1,\text{cell}}$, it is not always

necessary to construct a contrast agent that exhibits an increase in r_1 ; and that the cellular retention characteristics of contrast agents can be equally important. As cellular retention could potentially lead to elevated toxicity, intracellular contrast agents such as **8b** (ref. 12) and **9** (ref. 13) are likely to find applications as research tools rather than clinical diagnostics.

As mentioned before, it is desirable for a bimodal contrast agent to modulate both fluorescence intensities and relaxation rates upon the detection of a target. Metal ions are a particularly interesting case when used as analytes, in view of the rich chemistry involved in fluorescent metal ion detection. Using a bis-picolyl amine as the metal ion ligand, Zhang *et al.*¹⁴ described a contrast agent (**10**) which exhibits a quenched fluorescence and an increased relaxation rate upon binding Cu^{2+} ions. Whereas the appended naphthalimide is initially fluorescent, the paramagnetic nature of the d^9 ion quenches the fluorescence by either an electron transfer (eT) or energy transfer (ET) mechanism. As the Gd^{3+} ion (initially coordinated by the four DO3A nitrogen atoms, the three carboxylate ligands and up to two pyridines) competes with Cu^{2+} for the pyridine ligands, the resulting conformational change induces a change in the number of inner sphere water molecules (Fig. S1, ESI†). By this mechanism, the addition of three equivalents of Cu^{2+} leads to an increase in r_1 by 42% from $5.53 \text{ mM}^{-1} \text{ s}^{-1}$ at 0.5 T to $7.78 \text{ mM}^{-1} \text{ s}^{-1}$; while the fluorescence decreased by 92% after one equivalent of Cu^{2+} ions was added.

Jang *et al.*¹⁵ presented a bimodal contrast agent (**11**) based on a similar principle as complex **10**.¹⁴ Upon the addition of Cu^{2+} , the copper ions compete with Gd^{3+} for the carboxylate arms of an asymmetrically substituted diamionaphthalimide. Upon complexation with Cu^{2+} , the Gd-complex exhibits an increased q , resulting in an 100% increase in r_1 from $2.01 \text{ mM}^{-1} \text{ s}^{-1}$ to $4.01 \text{ mM}^{-1} \text{ s}^{-1}$ at 1.4 T and 37 °C. Whereas the addition of Zn^{2+} ions does moderately increase the fluorescence by chelation enhanced fluorescence (CHEF), preventing a photoinduced eT (PeT) process, the r_1 value was demonstrated only to be modulated by the addition of Cu^{2+} (Fig. 8 and Fig. S2, ESI†). This result suggests that in the case of Zn^{2+} , the coordination involves only ligands not coordinated by Gd^{3+} (*i.e.* nitrogen ligands), whereas Cu^{2+} is able to abstract carboxylates from the

Gd^{3+} -complex as well. The fluorescence is diminished by 56% upon addition of an equimolar amount Cu^{2+} . Furthermore, the contrast agent showed no significant toxicity in RAW 264.7 cells at concentrations up to 100 μM .

Both bimodal contrast agents **10**¹⁴ and **11**¹⁵ could find applications in the analysis of histological sections, providing the contrast agents exhibit the same specificity in a cellular environment, but the 7-coordinate chelate formed upon the addition of Cu^{2+} likely results in poor transmetalation stabilities, prohibiting *in vivo* applications.

2.2. Metal containing luminophores

In addition to bimodal contrast agents carrying an organic fluorophore, in recent years substantial progress in luminophores consisting of metal complexes has been made as well.

In 2012, two articles using a complex of Al^{3+} and three 8-hydroxyquinoline ligands as the luminophore were described. The hydroxyquinolines were further derivatised in the 5-position allowing for the attachment of a DO3A (**12**)¹⁶ or a DTTA mono amide (**13**)¹⁷ ligand, thus generating an AlGd_3 contrast agent. This type of contrast agent, consisting of a first generation dendrimer around a central metal ion is commonly referred to as a metallostar (Fig. 9). Both AlGd_3 metallostar agents (**12** and **13**) present a similar emission profile, exhibiting a broad emission from 400 nm to 700 nm with a maximum of 510 nm and 525 nm respectively. Apart from the fact that multimerisation leads to higher signal over noise ratios and that optical probes are more sensitive than magnetic probes, the multimerisation also accomplishes the synthesis of a larger molecule. Due to the increased hydrodynamic radius larger molecules exhibit slower tumbling rates and thus higher r_1 values. The formation of both contrast agents results in an increased r_1 , compared to the complexes before self-assembly around a central Al^{3+} ion. As the r_1 values of both contrast agents have been obtained at different field strengths, a direct comparison cannot be made.^{16,17}

Not only metal ions of p-block metals have shown to be useful, d-block metal complexes have been shown to be of particular interest as well. Generally, complexes of these metals will exhibit strong broad absorption bands in the visible region, and intense broad luminescence with tails into the NIR, due to the presence of metal-to-ligand charge transfer (MLCT) or ligand-to-metal charge transfer (LMCT) processes. Literature reports include a series of Zn-porphyrine complexes conjugated with Gd-DO3A mono amide (**14**),¹⁸ a TiGd_3 metallostar (**15**),¹⁹ a ReGd heterobimetallic complex (**16**),²⁰ and RuGd complexes,²¹ with either a linear Ru_2Gd architecture (**17**)^{21a} or a RuGd_3 metallostar architecture (**18**).^{21b,c}

In 2010, Song *et al.*¹⁸ described the synthesis of a series of Zn-porphyrine complexes conjugated with Gd-DO3A mono amide (**14**). Upon excitation of the Zn-porphyrine luminophore, light with wavelengths in the near-infrared (NIR) region of the electromagnetic spectrum is emitted. The light emitting scaffold was further used to add multiple Gd containing DO3A mono amide-based ligands. When comparing the r_1 values of probes **14a**, **14b** and **14c**, the r_1 per Gd ion increases from $4.2 \text{ mM}^{-1} \text{ s}^{-1}$ at 1.4 T and 37 °C over $10.5 \text{ mM}^{-1} \text{ s}^{-1}$ to

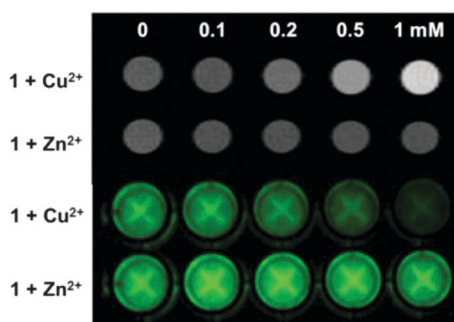


Fig. 8 T_1 -weighted phantom MR image (up) at 4.7 T, and fluorescence phantom image (down) of **11** (0.2 mM) in the presence of Cu^{2+} or Zn^{2+} ions with various concentrations (0–1 mM). Reprinted with permission from ref. 15. Copyright 2013 American Chemical Society.

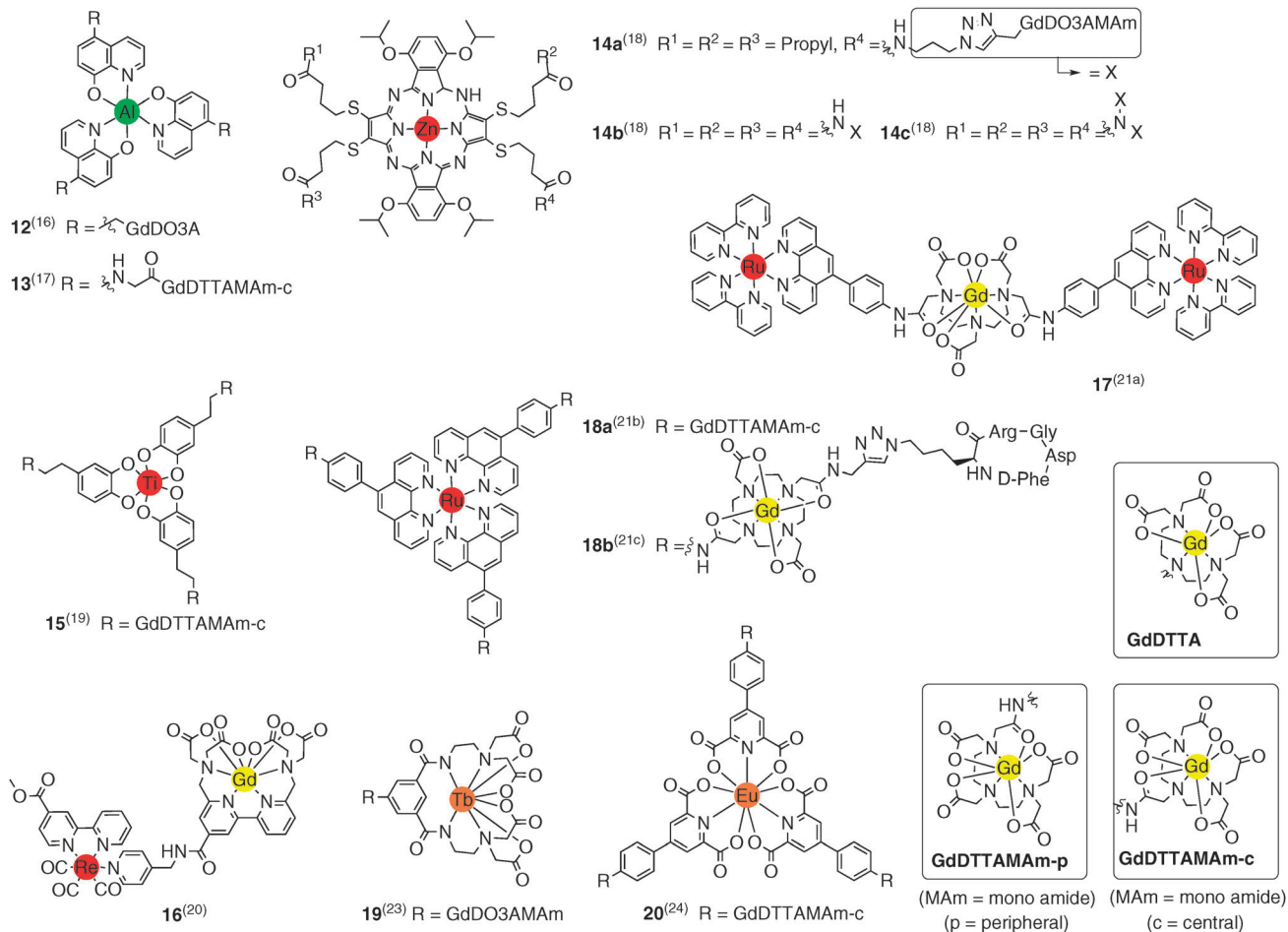


Fig. 9 Structures of metal containing luminophore MRI contrast agents **12–20**.^{16–24} (References between brackets.)

$12.8 \text{ mM}^{-1} \text{ s}^{-1}$; resulting in molecular r_1 values of $4.2 \text{ mM}^{-1} \text{ s}^{-1}$, $42 \text{ mM}^{-1} \text{ s}^{-1}$ and $102.4 \text{ mM}^{-1} \text{ s}^{-1}$ respectively.¹⁸

The TiGd_3 metallostar **15** exhibited a broad emission from 400 nm to 750 nm with a maximum at 490 nm upon excitation in the LMCT band at 380 nm. Due to the decreased tumbling rate of the large aggregate, a r_1 value of $12.3 \text{ mM}^{-1} \text{ s}^{-1}$ per Gd^{3+} ion and a molecular relaxivity of $36.9 \text{ mM}^{-1} \text{ s}^{-1}$ at 0.47 T and 37°C were obtained.¹⁹

ReGd complex **16** gave rise to bright luminescence from a $^3\text{MLCT}$ emission with a maximum intensity at 578 nm and a tail reaching well into the NIR, upon excitation into the MLCT band at 365 nm. At 0.47 T and 37°C the complex shows a r_1 value of $6.6 \text{ mM}^{-1} \text{ s}^{-1}$.²⁰

RuGd complexes **17**, **18a** and **18b** all share similar luminescence properties.²¹ Upon irradiation into the MLCT band (situated between 375 nm and 500 nm), a broad red emission from 525 nm with a tail reaching 850 nm and a maximum at around 610 nm can be observed. At 0.47 T and 37°C the complexes exhibit r_1 values of $7.2 \text{ mM}^{-1} \text{ s}^{-1}$, $12.0 \text{ mM}^{-1} \text{ s}^{-1}$ and $9.65 \text{ mM}^{-1} \text{ s}^{-1}$, respectively, resulting in molecular relaxivities of $7.2 \text{ mM}^{-1} \text{ s}^{-1}$, $36 \text{ mM}^{-1} \text{ s}^{-1}$, $28.95 \text{ mM}^{-1} \text{ s}^{-1}$. Metallostar **18b** is further decorated, using the Cu^{2+} catalysed click reaction, with cyclic RGD peptides. These peptides can

selectively recognise $\alpha_v\beta_3$ integrin, a cell surface receptor associated with tumour growth and atherosclerotic plaque formation. The recognition of the cell surface receptor with the RGD peptide decorated contrast agent slows the tumbling rate further down, resulting in an increased contrast (Fig. 10).^{21c} Binding $\alpha_v\beta_3$ integrin could lead to cellular internalisation of

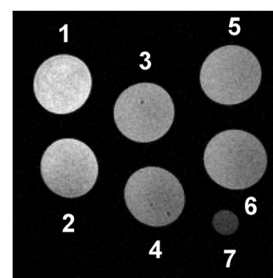


Fig. 10 T_1 -weighted MRI image of Jurkat T cells, incubated with **18b**, and a few control samples: (1) stimulated Jurkat T cells with **18b**; (2) nonstimulated Jurkat T cells with **18b**; (3) stimulated Jurkat T cells with GdDOTA; (4) nonstimulated Jurkat T cells with GdDOTA; (5) stimulated Jurkat T cells without contrast agent; (6) nonstimulated Jurkat T cells without contrast agent; and (7) phantom containing $50 \mu\text{M}$ GdDTPA (no cells). Reprinted with permission from ref. 21c. Copyright 2012 American Chemical Society.

the contrast agent, further studies are needed to determine the cellular localisation of the metallostar.

For contrast agents exhibiting slower tumbling rates, τ_m and τ_R reach a similar order of magnitude, therefore the tumbling rate is no longer the only major limiting factor determining r_1 . Amides of the carboxylic acids of DOTA and DTPA, synthetically being a convenient derivatisation method, give rise to elongation of τ_m caused by a change in the electron density of the carbonyl group. With this in mind, the difference in r_1 between **18a** and **18b**, exhibiting similar τ_R values (374 ± 5 ps and 469 ± 11 ps respectively), can be explained by the dramatic increase in τ_m from 122 ns in DOTA²² to 200 ns and 850 ns (all at 310 K), induced by the presence of one and two amide bonds in **18a** and **18b** respectively.²¹

Complementary to the broad MLCT and LMCT emissions arising from d-metal complexes, f-metals show a number of discrete sharp emission bands arising from f-f transitions. The design of a ligand that can serve both as a suitable ligand for MRI imaging (when using Gd³⁺ ions) and (NIR) optical imaging (when using for example Eu³⁺, Tb³⁺, Dy³⁺, Nd³⁺) has been shown to be feasible yet challenging. An identical bio-distribution can be assumed for both types of complexes, and can thus be considered bimodal, however these complexes are not covered in this tutorial review. Only bimodal complexes comprising a ligand, chelating both one or more Gd³⁺ ions and a second luminescent lanthanide, will be included to maintain clarity and for the sake of brevity.

Despite the promising results of bimodal lanthanide–lanthanide systems (in any definition of bimodality), they are associated with a disadvantage that at first sight might limit their applicability, *i.e.* they usually require excitation in the blue and UV regions of the electromagnetic spectrum (where tissues are not only impenetrable, the irradiation might also cause DNA damage). Yet the combination of these complexes with alternative optical sensitisation methods (*e.g.* upconverting nanoparticles (see later)) could overcome this issue.

In 2010, a DO3A mono amide–PADDTA (isophthalamide diethylene-diamminetetraacetate) conjugate (**19**) for the consecutive complexation of a Gd³⁺ and a Tb³⁺ ion was described.²³ The contrast agent showed a r_1 of $5.48 \text{ mM}^{-1} \text{ s}^{-1}$ in the absence of a second lanthanide ion and after the addition of a second lanthanide it showed no significant changes. The Gd–Tb hetero-bimetallic complex showed luminescence upon excitation of the ligand (at 297 nm) at 489 nm, 545 nm, 584 nm and 621 nm, which is consistent with the Tb³⁺ ion's $^5D_4 \rightarrow ^7F_J$ ($J = 3-6$) emission bands.

Recently, an EuGd₃ metallostar (**20**) has been shown to combine both high relaxivities and a sharp emission, particularly from the $^5D_0 \rightarrow ^7F_2$ band around 615 nm.²⁴ The r_1 per Gd³⁺ ion amounts to $9.6 \text{ mM}^{-1} \text{ s}^{-1}$ at 0.47 T and 37 °C, which results in a molecular relaxation rate of $28.8 \text{ mM}^{-1} \text{ s}^{-1}$.

Most of the inorganic complexes mentioned before represent a relatively facile route towards red and NIR luminophores, furthermore in many cases the construction of the luminophore adds to the relaxivity of the final complex. Yet despite some of these results, when compared to the organic conjugates, much less information regarding biological compatibility

and histological and cellular distribution is known. However, as some of the inorganic luminophores mentioned above are kinetically and thermodynamically stable, and their biological properties are also being assessed outside the scope of bimodal MRI/optical contrast agents, this knowledge discrepancy is likely to disappear in the near future.

We direct the reader to a very recent review concerning polymetallic lanthanide complexes with applications to bimodal imaging for further reading.²⁵

3. Supramolecular systems

3.1. Unique challenges

Examples of self-assembled bimodal systems include self-assembled bimodal systems (*e.g.* micelles and liposomes) and decorated nanosized objects. Whereas self-assembly or decorating nanoparticles results in the formation of large slowly rotating supramolecular systems, the construction of such molecular architectures presents some unique challenges as well.

Firstly, the supramolecular system rotates with a specific tumbling rate (τ_{Rg} , global rotational correlation time) and the complex rotates relative to the supramolecule (*e.g.* around the anchoring moiety) as well (τ_{Rl} , local rotational correlation time). As both processes contribute to the effective rotational correlation time, it is important to minimize local flexibility. These parameters are calculated using the Lipari–Szabo approach, with a specific order parameter S^2 , quantifying the degree of coupling between local and global rotations (with limiting values $S^2 = 1$, expressing only global rotation (completely rigid); and $S^2 = 0$, the contrast agent moves fully independently with regard to the nano-object). Due to the strong temperature dependence of τ_{Rl} , an increase in temperature usually results in a dramatic decrease in relaxivity.

Secondly, the contrast agent is partially buried in the supramolecular structure and the accessibility to water may be limited. As the molecule is no longer completely surrounded by water molecules, the number of second and outer sphere water molecules is reduced, diminishing their contribution to r_1 as well (Fig. 11).

Despite these limitations, supramolecular self-assembled MRI contrast agents represent an interesting class of contrast agents, as these typically consist of multiple MRI centers, resulting in high to very high overall r_1 values per nano-object. Due to a tumour's leaky blood vessels, nano-sized objects can permeate in the tumour tissue and reside there for elongated times due to an equally faulty lymph drainage system, which is known as the EPR (enhanced permeation and retention) effect.

From a synthetic point of view it should be also noted that most nano-objects cannot be characterised by the same methods or indeed to the same level of detail than their small molecule analogues. All nanoobjects, whether due to the synthesis of the core nanoobject or due to self-assembly exhibit inherent polydispersity. As small changes in reaction conditions may result in relatively poor reproducibility, translation into clinical practice may not be straightforward.

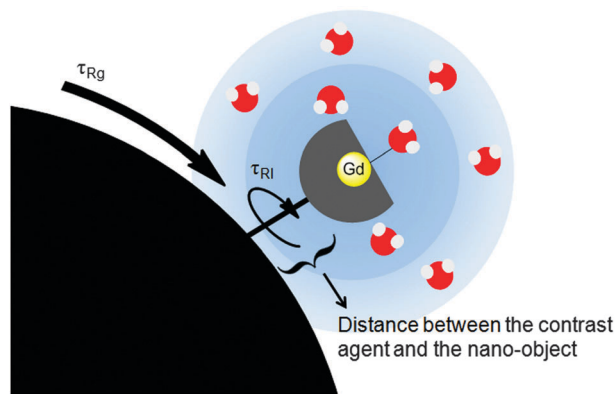


Fig. 11 The factors limiting the relaxivity of nano-conjugates. (Abbreviations: see main text.)

Biologically speaking, nano-objects are far less likely to be extravasated in the surrounding tissues after injection into the blood stream, with the exception of tumour targeted contrast agents utilising the EPR effect (as discussed above). This limits their use to the detection of blood-borne targets or targets along the excretion pathway. Small sized nano-objects (<30 nm) do not necessarily suffer from poor extravasation, but they are rapidly cleared from the bloodstream by renal excretion. Larger objects usually exhibit a much longer retention, and are removed from the blood mainly by hepatobiliary excretion. As mentioned above, the increased circulation time inherently leads to elevated toxicity profiles due to Gd^{3+} leaking. These issues decrease the applicability of nano-sized objects but do not necessarily represent an insurmountable hurdle. It is likely that future research will include contrast agents, either linked to a nano-object or self-assembled, that contain biologically degradable links. Hence the constructs fall apart in their constituents, resulting in faster excretion from the bloodstream.

3.2. Self-assembled structures

A first example of a self-assembled structure consists of a pyrene appended MRI contrast agent **21** (Fig. 12).²⁶ At concentrations above 0.60 mM, the contrast agent exhibits self-assembly into micellar structures with a population averaged hydrodynamic radius of 49 nm. Below the cmc, the contrast agent shows a r_1 value of $6.86 \pm 0.03 \text{ mM}^{-1} \text{ s}^{-1}$ at 25 °C and 0.47 T, excitation of the pyrene chromophore results in a highly structured emission in the 300–450 nm range. The micellar structure exhibits a r_1 of $33.11 \pm 0.04 \text{ mM}^{-1} \text{ s}^{-1}$, despite the fact that the structure exhibits significant flexibility ($S^2 = 0.24$). As a result of the formation of excimers (excited dimers), excitation of chromophores now results in the emission of a broad redshifted emission band with a maximum at 490 nm, and a tail > 600 nm.

In a second example of a micellar MRI contrast agent, the (*in casu* mixed) micelle consisted of 78 mol% dipalmitoyl-phosphatidylcholine (DPPC), 15.5 mol% Tween 80 (a surfactant) and 6.5 mol% of **22a** and **22b**.²⁷ The complexes were prepared with $\text{Gd}^{3+}/\text{Eu}^{3+}$ ratios ranging from 1:1 to 50:1. The optimal ratio, enabling both high r_1 and sufficient luminescence from

the $^5\text{D}_0 \rightarrow ^7\text{F}_J$ ($J = 0-4$) Eu^{3+} transitions, was determined to be 20:1. Under these conditions, **22a** exhibits a higher flexibility ($S^2 = 0.15-0.23$) than **22b** ($S^2 = 0.30-0.41$). The relaxivity of the **22b** containing micelles was determined to be $18.9 \text{ mM}^{-1} \text{ s}^{-1}$, $16.6 \text{ mM}^{-1} \text{ s}^{-1}$ and $12.4 \text{ mM}^{-1} \text{ s}^{-1}$ at 0.94 T and 25 °C, 37 °C and 50 °C respectively, clearly showing the influence of the temperature on the local rotation. Due to the presence of two anchoring groups, local rotation was limited, but as this necessitates the presence of two amides, τ_m is elevated (500 ns at 37 °C). The effect of the micellar architecture on the hydration of the complex was also demonstrated and it was calculated that only 3 second-sphere water molecules were present at 37 °C.

An early example of a liposomal formulation containing bimodal MRI contrast agents was published by Kamaly *et al.* in 2010, containing 5 mol% **23** in 100 nm micelles.²⁸ The relaxivity was reported to be $3.6 \text{ mM}^{-1} \text{ s}^{-1}$ at 4.7 T and 19 °C. Interestingly a similar micelle lacking the fluorescent rhodamine group showed a relaxivity of only $0.9 \text{ mM}^{-1} \text{ s}^{-1}$. The rhodamine molecule is thought to prevent the amphiphilic complex from burying itself too deeply in the lipid bilayer. The relatively low relaxivity is probably caused by a combination of local mobility and restriction of water accessibility. The liposomes were shown to exhibit cellular uptake and preferential localisation in tumour tissue caused by the EPR effect, as judged from fluorescence microscopy and T_1 MRI respectively.

Iqbal *et al.* presented the synthesis of small unilamellar liposomes **24** decorated with amines, allowing the conjugation of the NIR dye Cy5.5 and containing up to 40 mol% of Gd-DTPA-bis-oleate.²⁹ The bimodal liposomes were further decorated with antibodies with tumour homing properties. The liposomes showed relaxivities of $3.80 \pm 0.31 \text{ mM}^{-1} \text{ s}^{-1}$ and $4.30 \pm 0.95 \text{ mM}^{-1} \text{ s}^{-1}$ at 9.4 T for the 20% and 40% formulations, respectively, resulting in relaxivities of $2220 \pm 280 \text{ mM}^{-1} \text{ s}^{-1}$ and $23800 \pm 5270 \text{ mM}^{-1} \text{ s}^{-1}$ for the molar concentration of particles. The NIR dye Cy5.5 allowed for the detection of cellular uptake by confocal microscopy and tumour uptake by small-animal fluorescence imaging *in vivo*. A T_1 difference MRI of the antibody bearing liposomes clearly showed the location of brain tumours, as can be seen from Fig. 13.

The incorporation of anthracene, 1:1 $\text{Gd}^{3+}:\text{Nd}^{3+}$ **25**, and apolipoprotein E4 (ApoE4) in dimyristoylglycero-phosphatidylcholine (DMPC) based 60 nm liposomes allowed for the bimodal characterisation of these nano-particles.³⁰ Excitation of the anthracene moiety at 361 nm resulted in sensitized emission of sharp f-f transition bands of Nd^{3+} at 904, 1065 and 1335 nm (arising from $^4\text{F}_{3/2} \rightarrow ^4\text{I}_J$ ($J = 9/2, 11/2, 13/2$)). The Gd^{3+} containing liposomes were characterised by a r_1 of $43.9 \text{ mM}^{-1} \text{ s}^{-1}$ at 25 °C and 0.47 T. These remarkably high values were obtained partially due to the bis-hydrated nature of **25**. The incorporation of a drug in the liposome's cavity combined with the tumour targeting ability of ApoE4 could make this an interesting target for multimodal theranostic cancer treatment. In view of the toxicity of anthracene, more studies concerning the biodistribution and anthracene leakage *in vivo* will be necessary in order to fully assess the potential of this system as a theranostic.

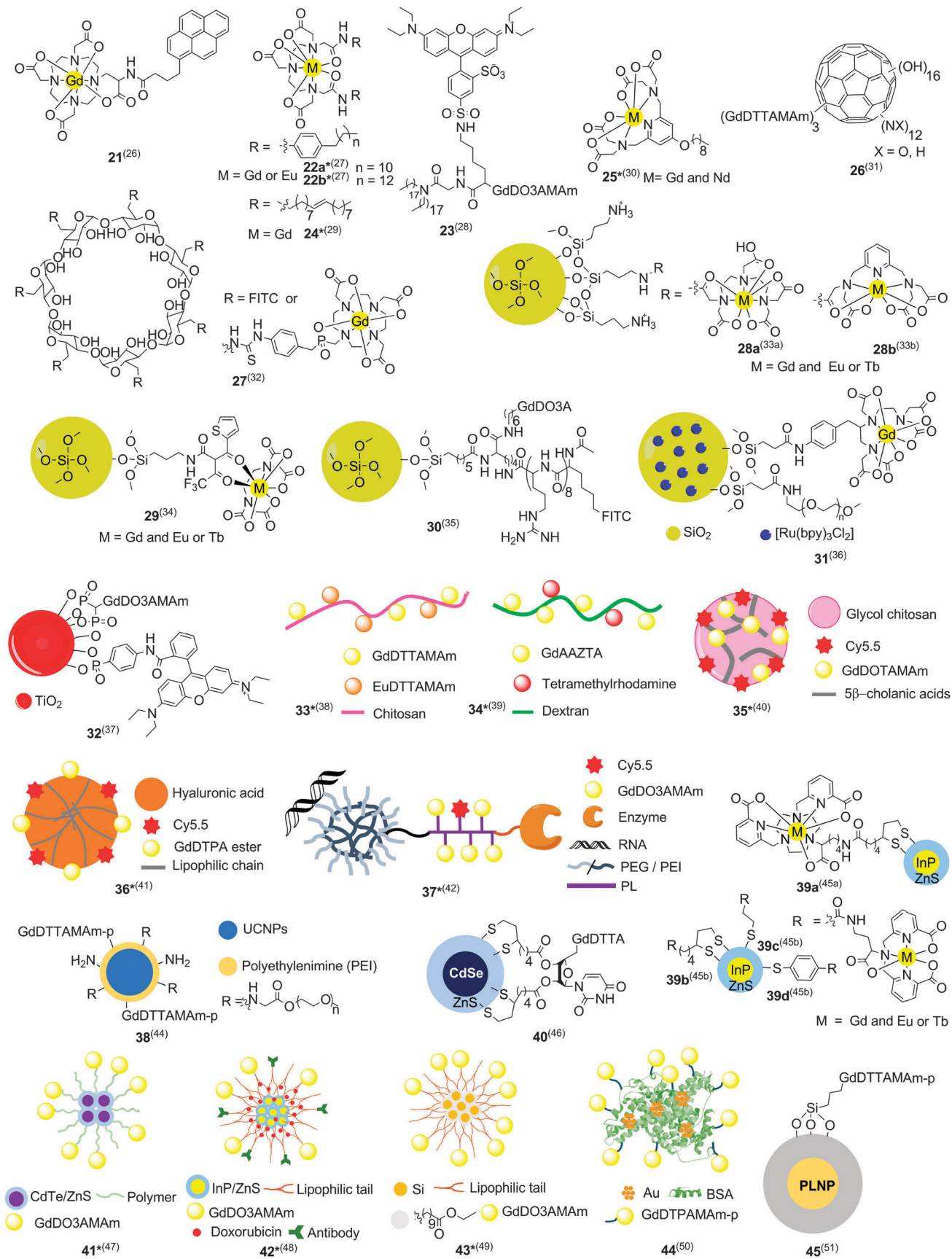


Fig. 12 Schematic representation of the supramolecular bimodal contrast agents 21–45.^{26–42,44–51} An expanded view of the structures marked with a star can be found in the ESI† (Fig. S3–S6) (see framed structures in Fig. 5 and 9 for complex abbreviations, references between brackets).

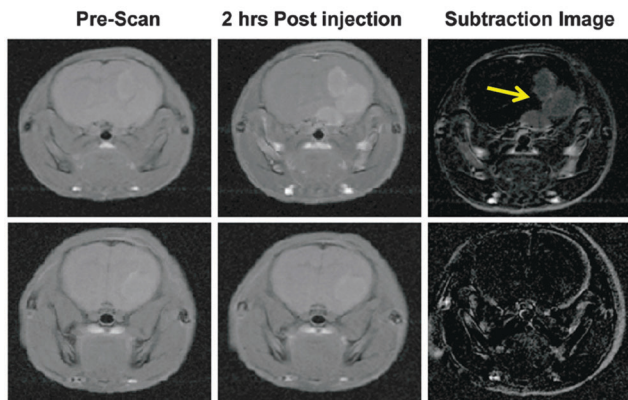


Fig. 13 T_1 weighted images of mice with brain tumors, following injection of **24** with (top) and without (bottom) antibodies for a tumour associated protein. Tumor location is indicated by a yellow arrow. Ref. 29. © IOP Publishing. Reproduced by permission of IOP Publishing. All rights reserved.

The C_{60} fullerene, bearing three Gd-DTPA mono amides (**26**), was designed as a bimodal theranostic agent for diseases caused by reactive oxygen species, as C_{60} can efficiently quench free radicals.³¹ The 250 nm-sized object, resulting from the self-assembly of the approximately 1 nm-sized fullerenes, showed fluorescence in the 400–650 nm region, with the exact range depending on the excitation wavelength. The relaxivity of $20.4 \text{ mM}^{-1} \text{ s}^{-1}$ at 0.5 T and 37°C clearly demonstrates the effectiveness of the contrast agent, as a result of the molecule's rigidity. Biodistribution studies revealed preferential targeting of the liver, albeit that this might just be an effect from the hepatobiliary excretion pathway, rather than active targeting.

3.3. Nano-object or polymer supported conjugates

As mentioned before, conjugating a contrast agent to a large object will ensure slow global tumbling rates, and it is this rationale that has led to the derivatisation of multiple nano-sized scaffolds with contrast agents.

In 2010, Kotková *et al.* described the reaction of a heptamino β -cyclodextrin with fluorescein isothiocyanate and the isothiocyanate derived from DO3AP, resulting in the statistical structure $(\text{GdL})_{6,9}\text{F}_{0,1}\text{-}\beta\text{-CD}$ **27**.³² The contrast agent reached a r_1 of $21.6 \text{ mM}^{-1} \text{ s}^{-1}$ at 0.47 T and 25°C by virtue of the rigid scaffold and the fast water exchange (caused by the phosphinate group) and the fluorescence was used to demonstrate the uptake and retention by mesenchymal stem cells.

A privileged scaffold in the design of nanoconjugates is based on silicon nanoparticles, due to the relative synthetic ease and low toxicity. In 2012 Pinho *et al.* published two papers using a 67 nm silicon nanoparticle as a scaffold, one bearing a DTPA mono amide **28a**, the other a pyridine containing ligand **28b**.³³ Whereas the luminescence of 1:1 $\text{Gd}^{3+}:\text{Eu}^{3+}$ or Tb^{3+} nanoparticles is dramatically increased in the case of **28b**, due to the sensitisation effect of the pyridine ligand, the relaxivity of the Gd^{3+} nanoparticles is relatively low in **28a** ($5.24 \text{ mM}^{-1} \text{ s}^{-1}$ at 0.47 T and 25°C) but even more so in **28b** ($2.70 \text{ mM}^{-1} \text{ s}^{-1}$), as can be expected due to the limited water

accessibility and high flexibility of the linkers grafting the complexes to the silicon surface. Both nanoparticles showed efficient cellular uptake in RAW 264.7 cells.

A similar approach has been used by Li *et al.* wherein heterocycle-appended diketone decorated $1 \mu\text{m}$ silicon particles were reacted with a 1:1 mixture of $\text{Gd}^{3+}:\text{Eu}^{3+}$ or Tb^{3+} and EDTA resulting in an exceptionally 10-coordinated Gd contrast agent (**29**).³⁴ Given that the nanoparticles bear bis-hydrated complexes ($q = 2$), the r_1 of $6.8\text{--}8.8 \text{ mM}^{-1} \text{ s}^{-1}$ at 9.4 T is also clearly limited by the flexibility. Whereas the use of EDTA and a diketone certainly is interesting from the point of view of structural diversity of contrast agents, the inherently lower stability of the chelates probably prohibits the applicability in a clinical setting.

Likewise the 123 nm bis-hydrated DO3A complex containing nanoparticle described by Joshi *et al.*³⁵ shows a r_1 of $6.9 \pm 0.7 \text{ mM}^{-1} \text{ s}^{-1}$ at 3.0 T, limited by local rotations. The particle was further substituted with a fluorescein or Cy5.5 chromophore and a cell-penetrating peptide (**30**), ensuring high efficacy in cellular uptake. The contrast agent showed remarkable tissue-selectivity for the lungs at a short timescale and for the lungs, spleen and liver after 24 h.

By decorating a 36 nm mixed silicon nanoparticle (doped with $\text{Ru}(\text{Bipy})_3$) with a more rigid linker ($S^2 = 0.46$) to a GdDTPA analogue (**31**), Lipani *et al.*³⁶ reported a bimodal contrast agent with high relaxivity ($\approx 30 \text{ mM}^{-1} \text{ s}^{-1}$ at 0.94 T and 37°C). As biological data of this contrast agent are currently not reported, their potential cannot be fully assessed. Yet the use of silicon nanoparticles with a luminophore entrapped within its structure represents an interesting route towards efficient bimodal MRI/optical contrast agents.

Other nanoparticles have been used as well, an interesting example is the titanium dioxide bimodal theranostic agent reported by Řehoř *et al.*³⁷ The 12 nm cell-penetrable TiO_2 particles were decorated with a phosphonate analogue of rhodamine and geminal bisphosphonate substituted Gd-DO3A mono amide complexes (**32**). The phosphonates cover the TiO_2 surface with high stability and the resulting bimodal contrast agent exhibits a r_1 of $28 \text{ mM}^{-1} \text{ s}^{-1}$ at 0.47 T and 25°C . Upon irradiation with UV-light the photo-catalytic activity of TiO_2 allowed for the production of reactive oxygen species, with possible applications in cancer therapy, provided that a solution can be found to reach similar results upon irradiation with longer wavelengths eliminating the need for direct UV irradiation.

Another strategy to increase the τ_R of a Gd-chelate contrast agent is by conjugation to a large (bio)polymer, a strategy employed by Chen *et al.*³⁸ who reported a chitosan-DTTA mono amide conjugate (**33**), containing a 1:1 ratio of Eu^{3+} and Gd^{3+} ions. Both luminescence and MRI images were shown but no details were reported.

Mamedov *et al.*³⁹ reported an AAZTA and tetramethyl-rhodamine conjugate of a 10 kDa dextran polymer (**34**). Despite the bis-hydrated ($q = 2$) nature, the r_1 was limited to $9.8 \text{ mM}^{-1} \text{ s}^{-1}$ at 3 T, which is most likely caused due to the flexible nature of the dextran.

In order to overcome the inherent flexibility of these biopolymers, the polymers can be conjugated with a lipophilic chain,

thus creating a polyamphiphilic molecule, adopting a more rigid core-shell conformation, with an inner lipophilic and outer hydrophilic composition. This strategy was used by Nam *et al.*⁴⁰ (35) and Cho *et al.*⁴¹ (36) using a chitosan backbone and a hyaluronic acid backbone, respectively. In the case of the chitosan particle, the relaxivity was considerably less than that of free GdDOTA, which is presumably caused by an unfavourable location of the conjugated Gd³⁺ complex in the lipophilic core, the hyaluronic acid conjugate on the other hand exhibited a r_1 of 19.8 mM⁻¹ s⁻¹ at 4.7 T, as the Gd³⁺ conjugate was now present on the surface of the nanoparticle. Making use of the targeting abilities of hyaluronic acid towards certain tumours, 36 clearly showed high tumour selectivity.⁴¹ The quite different results of these two nanoparticles, likely caused by a differential conformation, clearly demonstrate the difficulty in predicting the structure of supramolecular conjugates. Moreover, the inability to precisely characterise the conformation of the nanoparticles obligates assumptions to be made.

An elaborate biomodal theranostic contrast agent was reported in 2010,⁴² consisting of a polyethyleneglycol (PEG) chain grafted to a polyethyleneimine (PEI) chain, itself grafted to a poly-L-lysine (PL) chain bearing a terminal thiol. The PL was decorated with GdDOTA mono amides and Cy5.5. The PEI was used to electrostatically bind small interfering RNA (siRNA), with the potential to silence the expression of a tumour associated enzyme. The thiol was finally used to covalently attach a prodrug activating enzyme for dual tumour therapy (37). Whereas no specific details concerning the parameters governing r_1 were mentioned, both fluorescence and MRI tracking of the nanoparticles was reported. The enhanced anti-tumour activity of the drug (*vs.* reference molecules) was demonstrated by monitoring the tumour-growth over a period of 40 days, but more studies will be needed to assess long-term effects.

3.4. Luminescent nanoparticles

Whereas the luminescence in all previous examples originated from a small organic molecule or inorganic complex, the following section describes the use of luminescent nanoparticles, where the light-emission originates from the molecular structure of the nano-object itself. We direct the reader to a recent review for more detailed information concerning the mechanism behind the luminescence of the nano-objects described below.⁴³

A first example utilises an upconverting nanoparticle. Here the irradiation of light results in the emission of light with a shorter wavelength than the excitation wavelength, resulting from multiphoton processes. Applications arise from the possibility of excitation in the infrared and emission in the visible or NIR range. The reported nanoparticle was decorated with Gd-DTTA mono amide and PEG chains (38).⁴⁴ The resulting bimodal contrast agent showed a preferential biodistribution in the liver and spleen. A r_1 of 7.4 mM⁻¹ s⁻¹ at 1.4 T and 37 °C, twice that of free GdDTPA under the same conditions, was reported.

Quantum dots (QDs) are another interesting scaffold. A quantum dot is a small sized, typically 1–10 nm, crystal built from a semiconductor material. Due to the small size, the

excitons of the material are subject to quantum confinement, leading to photon emission with wavelengths in the visible area of the electromagnetic spectrum. QDs can exist as a core-shell structure, in which the shell protects the interior from external influences.

Stasiuk *et al.*⁴⁵ described the use of InP/ZnS quantum dots, with an emission wavelength at around 620 nm. The quantum dots were grafted with MRI contrast agents bearing a thiol or dithiol (39). The earliest reported conjugate (39a) bears a BPATCS based Gd³⁺ chelate ($q = 1$), whereas the bimodal contrast agents 39b–d bear a DPAA ligand ($q = 3$) exhibiting fast water exchange. The importance of the dependence of r_1 on both the hydration number (q) and the flexibility can be seen from the order of the r_1 with 39c (8.9 mM⁻¹ s⁻¹) < 39a (13 mM⁻¹ s⁻¹) < 39b (20.9 mM⁻¹ s⁻¹) < 39d (31.5 mM⁻¹ s⁻¹) at 0.81 T and 25 °C.

The addition of a bis-hydrated DTTA-uridine molecule to a CdSe/ZnS QD resulted in 40,⁴⁶ exhibiting luminescence at around 655 nm and a r_1 of 10.2 mM⁻¹ s⁻¹ at 4.7 T, 2.5-fold higher than the free DTTA-uridine complex.

By combining quantum dots with micelle formulations, nano-objects with larger sizes, vital for the maximisation of the EPR effect, can be created. Mixing CdTe/ZnS QDs emitting at 600 nm, with either a PEG based surfactant or a modified pluronic F127 (41), followed by the decoration of the outer surface resulted in r_1 values of 4.38 mM⁻¹ s⁻¹ and 8.17 mM⁻¹ s⁻¹ at 4.7 T respectively.⁴⁷ A similar strategy using InP/ZnS QDs (emission at 645 nm) and a mPEG-DSPE amphiphile was used by Hu *et al.*⁴⁸ (42). No quantification of the relaxivity of the resulting nanoparticle was reported but T_1 weighted MRI images showed a brighter image. The micelles were further loaded with doxorubicin, and the EPR effect allowed for the preferential delivery to tumour tissues.

In order to limit the inherent toxicity of nanoparticles constructed from heavy metals, Erogbogbo *et al.*⁴⁹ proposed to use silicon based luminescent QDs. Whereas the luminescent properties of the QDs (emission maximum at 750 nm) are ideal for tissue penetration, 43 however required excitation in the UV region. Potentially this type of QDs could be excited by multiphoton excitation, shifting the excitation wavelength to the red and NIR regions of the electromagnetic spectrum. Though this was not experimentally validated for this specific contrast agent. The relaxivity is also dramatically lowered by conjugating with the micelle's terminal amines ($r_1 = 2.43$ mM⁻¹ s⁻¹ at 4.7 T and 25 °C), *vs.* for example 41,⁴⁷ suggesting that the MRI complexes may be buried within the micelle.⁴⁹

Gold nanoclusters, consisting of only a few of gold atoms, exhibit luminescent properties reminiscent of molecular fluorescence, as they exhibit a HOMO (highest occupied molecular orbital)–LUMO (lowest unoccupied molecular orbital) bandgap, similar to small molecules. By constructing bovine serum albumin (BSA) supported gold clusters, conjugated with DTTA mono amide, Sun *et al.*⁵⁰ reported a bimodal contrast agent (44) showing fluorescence centred around 650 nm, whilst allowing for high contrast, with a r_1 of 23.7 mM⁻¹ s⁻¹ at 1.5 T.

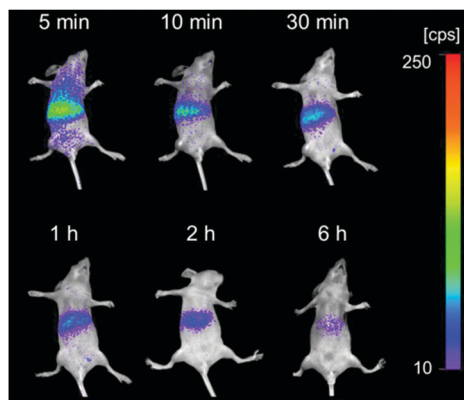


Fig. 14 *In vivo* NIR luminescence images of a normal mouse after intravenous injection of pre-irradiated **45**. Reprinted with permission from ref. 51. Copyright 2014 American Chemical Society.

A very promising recent addition to these bimodal luminescent nanoparticles is represented by the work of Abdulkayum *et al.*⁵¹ utilising the so called persistent luminescent nanoparticles (PLNP). This class of nanoparticles, in contrast to quantum dots, exhibits very slow luminescence decay. This allows for the pre-irradiation of the nanoparticles and the subsequent detection in the absence of an excitation source. The utilised PLNP (**45**) is characterised by a remarkable Stokes' shift (the difference between the absorption and emission maximum) of 450 nm. The PLNP are irradiated prior to their administration, elegantly bypassing problems associated with the excitation wavelength of 254 nm. However, the relaxivity is smaller than some of the other similar sized objects ($r_1 = 6.7 \text{ mM}^{-1} \text{ s}^{-1}$ at 1.2 T and 30 °C). Biodistribution studies revealed the preferential localisation in the liver, both by T_1 weighted imaging and NIR imaging, which is likely due to the hepatobiliary excretion pathway and is not surprising in view of the absence of any targeting groups on the surface of the PLNP. The NIR imaging of mice injected with pre-irradiated **45** demonstrated that the luminescence can be detected up to 6 hours subsequent to UV irradiation (Fig. 14).

4. Conclusion

Bimodal optical/MRI contrast agents based on Gd^{3+} chelates exist in a wide diversity of morphologies, each one with its own advantages as well as limitations. Small-molecule probes allow for the construction of precisely defined structures, enabling characterisation with methods, commonly used in organic and inorganic syntheses. Due to the relatively small scale and the relatively fast tumbling rate associated therewith, the relaxivity may be limited. Nanoscale systems on the other hand allow for the construction of bimodal contrast agents with slow global tumbling rates. However, local flexibility and limited water accessibility may result. Furthermore, characterisation methods allowing for the precise determination of the structure are lacking and possible reproducibility issues are current challenges. On the other hand, the nanosized objects present a convenient platform

for theranostics, allowing for the simultaneous delivery of drugs to certain tissues as well as the bimodal tracking of the delivery. Given these pros and cons, the choice of the contrast agent's architecture depends highly on the desired applications and must be chosen judiciously.

With this tutorial review we hope to spark the interest of students and entice the scientific community into developing new generations of high relaxivity and brightly luminescent bimodal contrast agents.

Acknowledgements

This work was supported by the Creative Research Initiative program (No. 2009-0081566) of the National Research Foundation of Korea (JSK) and the Korea University Researcher Support Program (PV).

Notes and references

- (a) A. Louie, *Chem. Rev.*, 2010, **110**, 3146; (b) C. S. Bonnet and É. Tóth, *C. R. Chim.*, 2010, **13**, 700.
- (a) P. Caravan, J. J. Ellison, T. J. McMurry and R. B. Lauffer, *Chem. Rev.*, 1999, **99**, 2293; (b) P. Caravan, C. T. Farrar, L. Frullano and R. Uppal, *Contrast Media Mol. Imaging*, 2009, **4**, 89; (c) H. Friebohn, *Basic one- and two-dimensional NMR spectroscopy*, Wiley-VCH, Weinheim, 5th edn, 2011; (d) D. Weishaupt, V. D. Köchli and B. Marincek, *How does MRI work?: an introduction to the physics and function of magnetic resonance imaging*, Springer, Berlin, New York, 2nd edn, 2006; (e) A. Merbach, L. Helm and É. Tóth, *The Chemistry of Contrast Agents in Medical Magnetic Resonance Imaging*, John Wiley & Sons, Ltd, Chichester, UK, 2nd edn, 2013.
- (a) E. L. Que and C. J. Chang, *Chem. Soc. Rev.*, 2010, **39**, 51; (b) G.-L. Davies, I. Kramberger and J. J. Davis, *Chem. Commun.*, 2013, **49**, 9704; (c) M. C. Heffern, L. M. Matosziuk and T. J. Meade, *Chem. Rev.*, 2014, **114**, 4496.
- T. Leiner and W. Kucharczyk, *J. Magn. Reson. Imaging*, 2009, **30**, 1233 and references therein.
- (a) N. Sim, S. Gottschalk, R. Pal, J. Engelmann, D. Parker and A. Mishra, *Chem. Sci.*, 2013, **4**, 3148; (b) A. Mishra, R. Mishra, S. Gottschalk, R. Pal, N. Sim, J. Engelmann, M. Goldberg and D. Parker, *ACS Chem. Neurosci.*, 2014, **5**, 128.
- R. Uppal, K. L. Ciesienski, D. B. Chonde, G. S. Loving and P. Caravan, *J. Am. Chem. Soc.*, 2012, **134**, 10799.
- (a) L. Frullano, C. Wang, R. H. Miller and Y. Wang, *J. Am. Chem. Soc.*, 2011, **133**, 1611; (b) L. Frullano, J. Zhu, C. Wang, C. Wu, R. H. Miller and Y. Wang, *J. Med. Chem.*, 2012, **55**, 94.
- S. M. Vithanarachchi and M. J. Allen, *Chem. Commun.*, 2013, **49**, 4148.
- (a) A. F. Martins, J.-F. Morfin, C. F. G. C. Geraldés and É. Tóth, *J. Biol. Inorg. Chem.*, 2014, **19**, 281; (b) A. F. Martins, J.-F. Morfin, A. Kubičková, V. Kubiček, F. Buron, F. Suzenet, M. Salerno, A. N. Lazar, C. Duyckaerts, N. Arlicot,

- D. Guilloteau, C. F. G. C. Geraldles and É. Tóth, *ACS Med. Chem. Lett.*, 2013, **4**, 436.
- 10 J. E. Jones, A. J. Amoroso, I. M. Dorin, G. Parigi, B. D. Ward, N. J. Burma and S. J. A. Pope, *Chem. Commun.*, 2011, **47**, 3374.
- 11 H.-K. Kim, M.-K. Kang, K.-H. Jung, S.-H. Kang, Y.-H. Kim, J.-C. Jung, G. H. Lee, Y. Chang and T.-J. Kim, *J. Med. Chem.*, 2013, **56**, 8104.
- 12 C. Rivas, G. J. Stasiuk, J. Gallo, F. Minuzzi, G. A. Rutter and N. J. Long, *Inorg. Chem.*, 2013, **52**, 14284.
- 13 A. Keliris, T. Ziegler, R. Mishra, R. Pohmann, M. G. Sauer, K. Ugurbil and J. Engelmann, *Bioorg. Med. Chem.*, 2011, **19**, 2529.
- 14 X. Zhang, X. Jing, T. Liu, G. Han, H. Li and C. Duan, *Inorg. Chem.*, 2012, **51**, 2325.
- 15 J. H. Jang, S. Bhuniya, J. Kang, A. Yeom, K. S. Hong and J. S. Kim, *Org. Lett.*, 2013, **15**, 4702.
- 16 W.-S. Li, J. Luo, F. Jiang and Z.-N. Chen, *Dalton Trans.*, 2012, **41**, 9405.
- 17 E. Debroye, G. Dehaen, S. V. Eliseeva, S. Laurent, L. Vander Elst, R. N. Muller, K. Binnemans and T. N. Parac-Vogt, *Dalton Trans.*, 2012, **41**, 10549.
- 18 Y. Song, H. Zong, E. R. Trivedi, B. J. Vesper, E. A. Waters, A. G. M. Barrett, J. A. Radosevich, B. M. Hoffman and T. J. Meade, *Bioconjugate Chem.*, 2010, **21**, 2267.
- 19 G. Dehaen, S. V. Eliseeva, K. Kimpe, S. Laurent, L. Vander Elst, R. N. Muller, W. Dehaen, K. Binnemans and T. N. Parac-Vogt, *Chem. – Eur. J.*, 2012, **18**, 293.
- 20 A. Boulay, S. Laine, N. Leygue, E. Benoist, S. Laurent, L. Vander Elst, R. N. Muller, B. Mestre-Voegtli and C. Picard, *Tetrahedron Lett.*, 2013, **54**, 5395.
- 21 (a) G. Dehaen, P. Verwilt, S. V. Eliseeva, S. Laurent, L. Vander Elst, R. N. Muller, W. M. De Borggraeve, K. Binnemans and T. N. Parac-Vogt, *Inorg. Chem.*, 2011, **50**, 10005; (b) G. Dehaen, S. V. Eliseeva, P. Verwilt, S. Laurent, L. Vander Elst, R. N. Muller, W. De Borggraeve, K. Binnemans and T. N. Parac-Vogt, *Inorg. Chem.*, 2012, **51**, 8775; (c) P. Verwilt, S. V. Eliseeva, L. Vander Elst, C. Burtea, S. Laurent, S. Petoud, R. N. Muller, T. N. Parac-Vogt and W. M. De Borggraeve, *Inorg. Chem.*, 2012, **51**, 6405.
- 22 (a) S. Laurent, L. Vander Elst and R. N. Muller, *Contrast Media Mol. Imaging*, 2006, **1**, 128; (b) D. H. Powell, O. M. N. Dhubhghaill, D. Pubanz, L. Helm, Y. S. Lebedev, W. Schlaepfer and A. E. Merbach, *J. Am. Chem. Soc.*, 1996, **118**, 9333.
- 23 I. Mamedov, T. N. Parac-Vogt, N. K. Logothetis and G. Angelovski, *Dalton Trans.*, 2010, **39**, 5721.
- 24 E. Debroye, M. Ceulemans, L. Vander Elst, S. Laurent, R. N. Muller and T. N. Parac-Vogt, *Inorg. Chem.*, 2014, **53**, 1257.
- 25 E. Debroye and T. N. Parac-Vogt, *Chem. Soc. Rev.*, 2014, **43**, 8178.
- 26 M. F. Ferreira, G. Pereira, A. F. Martins, C. I. O. Martins, M. I. M. Prata, S. Petoud, É. Tóth, P. M. T. Ferreira, J. A. Martins and C. F. G. C. Geraldles, *Dalton Trans.*, 2014, **43**, 3162.
- 27 E. Debroye, S. V. Eliseeva, S. Laurent, L. Vander Elst, R. N. Muller and T. N. Parac-Vogt, *Dalton Trans.*, 2014, **43**, 3589.
- 28 N. Kamaly, T. Kalber, G. Kenny, J. Bell, M. Jorgensen and A. Miller, *Org. Biomol. Chem.*, 2010, **8**, 201.
- 29 U. Iqbal, H. Albaghdadi, M.-P. Nieh, U. I. Tuor, Z. Mester, D. Stanimirovic, J. Katsaras and A. Abulrob, *Nanotechnology*, 2011, **22**, 195102.
- 30 S. Lacerda, C. S. Bonnet, A. Pallier, S. Villette, F. Foucher, F. Westall, F. Buron, F. Suzenet, C. Pichon, S. Petoud and É. Tóth, *Small*, 2013, **9**, 2662.
- 31 M. Zhen, J. Zheng, Y. Wang, C. Shu, F. Gao, J. Zou, I. Pyykkö and C. Wang, *Chem. – Eur. J.*, 2013, **19**, 14675.
- 32 Z. Kotková, J. Kotek, D. Jiráček, P. Jendelová, V. Herynek, Z. Berková, P. Hermann and I. Lukeš, *Chem. – Eur. J.*, 2010, **16**, 10094.
- 33 (a) S. L. C. Pinho, H. Faneca, C. F. G. C. Geraldles, J. Rocha, L. D. Carlos and M.-H. Delville, *Eur. J. Inorg. Chem.*, 2012, 2828; (b) S. L. C. Pinho, H. Faneca, C. F. G. C. Geraldles, M.-H. Delville, L. D. Carlos and J. Rocha, *Biomaterials*, 2012, **33**, 925.
- 34 Y.-Y. Li, B. Yan and Q.-P. Li, *Dalton Trans.*, 2013, **42**, 1678.
- 35 R. Joshi, V. Feldmann, W. Koestner, C. Detje, S. Gottschalk, H. A. Mayer, M. G. Sauer and J. Engelmann, *Biol. Chem.*, 2013, **394**, 125.
- 36 E. Lipani, S. Laurent, M. Surin, L. Vander Elst, P. Leclère and R. N. Muller, *Langmuir*, 2013, **29**, 3419.
- 37 I. Řehoř, V. Vilímová, P. Jendelová, V. Kubíček, D. Jiráček, V. Herynek, M. Kapcalová, J. Kotek, J. Černý, P. Hermann and I. Lukeš, *J. Med. Chem.*, 2011, **54**, 5185.
- 38 B. Chen, Y. Li, B. Zhang, B. Zhang, Y. Wu and D. Shi, *Adv. Mater. Res.*, 2011, **266**, 118.
- 39 I. Mamedov, J. Engelmann, O. Eschenko, M. Beyerlein and N. K. Logothetis, *Chem. Commun.*, 2012, **48**, 2755.
- 40 T. Nam, S. Park, S.-Y. Lee, K. Park, K. Choi, I. C. Song, M. H. Han, J. J. Leary, S. A. Yuk, I. C. Kwon, K. Kim and S. Y. Jeong, *Bioconjugate Chem.*, 2010, **21**, 578.
- 41 H.-J. Cho, H. Y. Yoon, H. Koo, S.-H. Ko, J.-S. Shim, J.-H. Cho, J. H. Park, K. Kim, I. C. Kwon and D.-D. Kim, *J. Controlled Release*, 2012, **162**, 111.
- 42 C. Li, M.-F. Penet, F. Wildes, T. Takagi, Z. Chen, P. T. Winnard, D. Artemov and Z. M. Bhujwalla, *ACS Nano*, 2010, **4**, 6707.
- 43 J. Yao, M. Yang and Y. Duan, *Chem. Rev.*, 2014, **114**, 6130.
- 44 Y. Wang, L. Ji, B. Zhang, P. Yin, Y. Qiu, D. Song, J. Zhou and Q. Li, *Nanotechnology*, 2013, **24**, 175101.
- 45 (a) G. J. Stasiuk, S. Tamang, D. Imbert, C. Poillot, M. Giardiello, C. Tisseyre, E. L. Barbier, P. H. Fries, M. de Waard, P. Reiss and M. Mazzanti, *ACS Nano*, 2011, **5**, 8193; (b) G. J. Stasiuk, S. Tamang, D. Imbert, C. Gateau, P. Reiss, P. Fries and M. Mazzanti, *Dalton Trans.*, 2013, **42**, 8197.
- 46 J. Park, S. Bhuniya, H. Lee, Y.-W. Noh, Y. T. Lim, J. H. Jung, K. S. Hong and J. S. Kim, *Chem. Commun.*, 2012, **48**, 3218.

- 47 L. Liu, W.-C. Law, K.-T. Yong, I. Roy, H. Ding, F. Erogbogbo, X. Zhang and P. N. Prasad, *Analyst*, 2011, **136**, 1881.
- 48 R. Hu, Y. Wang, X. Liu, G. Lin, C. H. Tan, W.-C. Law, I. Roy and K.-T. Yong, *RSC Adv.*, 2013, **3**, 8495.
- 49 F. Erogbogbo, C.-W. Chang, J. L. May, L. Liu, R. Kumar, W.-C. Law, H. Ding, K. T. Yong, I. Roy, M. Sheshadri, M. T. Swihart and P. N. Prasad, *Nanoscale*, 2012, **4**, 5483.
- 50 G. Sun, L. Zhou, Y. Liu and Z. Zhao, *New J. Chem.*, 2013, **37**, 1028.
- 51 A. Abdukayum, C.-X. Yang, Q. Zhao, J.-T. Chen, L.-X. Dong and X.-P. Yan, *Anal. Chem.*, 2014, **86**, 4096.